Journal of Biomedical Optics

BiomedicalOptics.SPIEDigitalLibrary.org

Target-to-background enhancement in multispectral endoscopy with background autofluorescence mitigation for quantitative molecular imaging

Chenying Yang
Vivian W. Hou
Emily J. Girard
Leonard Y. Nelson
Eric J. Seibel

SPIE.

Target-to-background enhancement in multispectral endoscopy with background autofluorescence mitigation for quantitative molecular imaging

Chenying Yang,[a] Vivian W. Hou,[b] Emily J. Girard,[c] Leonard Y. Nelson,[d] and Eric J. Seibel[d,*]
[a]University of Washington, Department of Bioengineering, Seattle, Washington 98195, United States
[b]University of Washington, Department of Biology, Seattle, Washington 98195, United States
[c]Fred Hutchinson Cancer Research Center, Clinical Research Division, Seattle, Washington 98109, United States
[d]University of Washington, Department of Mechanical Engineering, Seattle, Washington 98195, United States

Abstract. Fluorescence molecular imaging with exogenous probes improves specificity for the detection of diseased tissues by targeting unambiguous molecular signatures. Additionally, increased diagnostic sensitivity is expected with the application of multiple molecular probes. We developed a real-time multispectral fluorescence-reflectance scanning fiber endoscope (SFE) for wide-field molecular imaging of fluorescent dye-labeled molecular probes at nanomolar detection levels. Concurrent multichannel imaging with the wide-field SFE also allows for real-time mitigation of the background autofluorescence (AF) signal, especially when fluorescein, a U.S. Food and Drug Administration approved dye, is used as the target fluorophore. Quantitative tissue AF was measured for the *ex vivo* porcine esophagus and murine brain tissues across the visible and near-infrared spectra. AF signals were then transferred to the unit of targeted fluorophore concentration to evaluate the SFE detection sensitivity for sodium fluorescein and cyanine. Next, we demonstrated a real-time AF mitigation algorithm on a tissue phantom, which featured molecular probe targeted cells of high-grade dysplasia on a substrate containing AF species. The target-to-background ratio was enhanced by more than one order of magnitude when applying the real-time AF mitigation algorithm. Furthermore, a quantitative estimate of the fluorescein photodegradation (photobleaching) rate was evaluated and shown to be insignificant under the illumination conditions of SFE. In summary, the multichannel laser-based flexible SFE has demonstrated the capability to provide sufficient detection sensitivity, image contrast, and quantitative target intensity information for detecting small precancerous lesions *in vivo*. [DOI: 10.1117/1.JBO.19.7.076014]

Keywords: fluorescence; molecular diagnostic imaging; wide-field fluorescence imaging; flexible endoscopy; scanning fiber endoscope; multispectral imaging; autofluorescence; target-to-background ratio; fluorescein; cancer detection; real-time imaging; contrast enhancement.

Paper 140141R received Mar. 4, 2014; revised manuscript received Jun. 18, 2014; accepted for publication Jun. 25, 2014; published online Jul. 15, 2014.

1 Introduction

Optical molecular endoscopic imaging with the administration of exogenous fluorophore probes has become an area of great interest in many clinical diagnostic and surgical applications.[1–6] Numerous endoscopic applications for tracking exogenous targeted fluorescence are under investigation, such as detection and diagnosis of early cancerous lesions in Barrett's esophagus,[7] navigation and demarcation of tumor margins during brain surgery,[8,9] and detection of early neoplasia in oral tissue,[10] lung,[11] bladder,[12] and smaller gastrointestinal (GI) ducts.[13] Moreover, translational studies for first-in-human application of fluorescence molecular targets have been demonstrated in colonic dysplasia detection as well as surgical guidance for ovarian cancer.[14,15] Compared to other optical contrast imaging techniques such as narrow band imaging and autofluorescence (AF) imaging, fluorescence molecular imaging with exogenous probes improves specificity for the detection of diseased tissues by targeting specific molecular entities such as overexpressed cell surface proteins at the cellular level.[1,2] Meanwhile, due to the heterogeneity of the disease molecular profile across individual patients, diagnostic sensitivity is expected to increase with the application of multiple molecular specific targeting using a panel of fluorescence probes.[16,17]

Many cancers are treatable by ablation or resection if detected at a very early stage. The problem in conventional white-light imaging is the lack of disease-specific optical signatures to localize and visualize the precancerous lesion.[18] Detection is further hindered by the diffuse and patchy nature of the lesions, which are often composed of distributed clusters of cells.[16,19] This leads to one of the major challenges for the clinical realization of fluorescence molecular imaging, which is the requirement for high detection sensitivity *in vivo* to locate suspect tissue areas.[20,21] The sensitivity required for identifying small and sparse early cancerous lesions in routine endoscopic surveillance and the delineation of residue malignant cancer cells during surgical operations are critical in reducing tumor occurrence and increasing the survival rate. Thus, increasing contrast in real-time intraoperative imaging has become a critical factor in the design and quality assurance of a fluorescence molecular imaging approach for translation to clinical diagnosis and therapy.

*Address all correspondence to: Eric J. Seibel, eseibel@uw.edu

0091-3286/2014/$25.00 © 2014 SPIE

Detection sensitivity of an exogenous fluorophore probe is limited by three major factors: first, the characteristics of the molecular probe, such as probe-tissue binding affinity, nonspecific binding and diffusion coefficient, as well as characteristics of the fluorophore, such as quantum efficiency, absorption coefficient, fluorescence wavelength, and photodegradation (also known as photobleaching) rates.[22–26] Second, the device performance and its detection sensitivity must be designed for each molecular target.[21] Last, the tissue AF background that degrades image contrast must be addressed.[20]

For sensitive and specific early cancer targeting in clinical applications, many fluorescent molecular probes are currently under development.[3,27,28] These molecular probes target biomarkers indicative of early disease stages using antibodies or peptides, and are conjugated with a fluorescent indicator dye or nanoparticle. One of the best fluorophores for this purpose is fluorescein. In many respects this dye is preferable to the near-infrared (NIR) dyes under development due to its status as a U.S. Food and Drug Administration (FDA)-approved dye with high molar absorptivity, fluorescence quantum yield >90%, good water solubility, and an overall lower price when compared to NIR dyes.[25,29] Meanwhile, a significantly increased photostability and pH-independent quantum yield of fluorescein derivatives have been reported in recent publications.[30,31] Methylene blue and indocyanine green (ICG) are red-NIR dyes that are FDA approved for clinical use and take advantage of deeper light penetration at a red-NIR illumination of 650 and 760 nm, respectively.[32] However, fluorescein dye is not widely used even for surface imaging applications, largely because it suffers from a low target-to-background ratio (T/B), which is caused by a high degree of tissue background AF that overlaps the dye emission in the green spectral range.

It has been reported that the tissue AF often masks exogenous molecular probe fluorescence signal and, thus, limits the actual detection T/B *in vivo*.[15,33–37] Other than fluorescein, a targeting probe sensitive to cellular glucose metabolism, 2-(N-(7-nitrobenz-2-oxa-1,3-diazol-4-yl)amino)-2-deoxyglucose (2-NBDG), a fluorescent analog to 2-deoxy-2 ((18)F) fluoro-D-glucose, which is routinely used in positron emission tomography for molecular imaging, has been shown as a promising candidate in optical molecular imaging translatable from bench to bed.[10,38] However, 2-NBDG also suffers from a significant masking effect from the background AF in the green spectral region.[39,40]

Recently, efforts have been directed at the advancement of molecular imaging devices by improving the fluorescence detection sensitivity of the imaging device through evaluations based on *in vitro* imaging of low concentrations of the targeting probe.[41,42] However, in *in vivo* clinical applications, the tissue background AF signal can exceed the device's detection sensitivity measured from the *in vitro* method, which renders meaningless the engineering efforts to increase a device's detection sensitivity limit. Therefore, any device will be limited to the AF background unless an approach to mitigate the AF can be implemented on the device. Meanwhile, understanding the quantitative spectroscopic characteristics of the targeted tissue's AF background is essential to the success of a viable fluorescence molecular imaging device. In the current study, we develop an approach to mitigate the AF background problem and apply this improvement to a high-sensitivity, ultrathin, and flexible multispectral fluorescence endoscopic device.

For two specific fluorescence-guided clinical applications—endoscopic early cancer detection in Barrett's esophagus, and surgical brain tumor demarcation and resection—*ex vivo* porcine esophagus and wild-type murine brain tissue were used to study the levels of background tissue AF. The porcine esophagus was chosen because its morphology, histology, and biochemistry are similar to that of humans and, therefore, it represents a good model for the human esophagus tissue.[43] Likewise, the wild-type mouse (nu/nu) was used as the healthy control of a patient-derived tumor xenograft mouse model of brain tumors. AF signals from the two types of tissue were quantitatively compared *ex vivo* with a gold standard quantitative imaging device and transferred into a physical standard based on the exogenous molecular probe fluorophore concentration, defined as the autofluorescence equivalent concentration (AEC). The detection sensitivity of the multispectral fluorescence endoscope was then evaluated in visible and NIR spectra using both AEC and low-concentration low-volume fluorophore dilutions. Furthermore, based on quantitative evaluation of target tissue AF, a real-time AF mitigation algorithm was implemented which significantly increased the T/B for a fluorescein conjugated molecular probe and 2-NGDB in a wide-field fluorescence imaging endoscope by 44- to 56-fold. Together, nanomolar sensitivity combined with a T/B ratio >80 was achieved with the newly developed multispectral ultrathin and flexible scanning fiber endoscope (SFE), and was demonstrated in an *in vitro* study using molecular targets of high-grade dysplasia and esophageal adenocarcinoma on a tissue phantom.

2 Materials and Methods

2.1 *Multispectral SFE System*

The new multispectral SFE system was specifically designed and engineered for wide-field, high-resolution, and real-time fluorescence molecular imaging and navigation.[44] Compared to a conventional endoscopic passive imaging system using diffuse white-light illumination, the multispectral SFE incorporates three low-power diode lasers: 448, 488, and 642 nm (FiberTec™, Blue Sky Research, Milpitas, California) that can be jointly or selectively launched at the base station and sent to the distal end of SFE via a single-mode optical fiber using a custom optical fiber combiner (Wave Division Multiplexer, Oz Optics, Ottawa, Ontario, Canada). In the current study, a 448-nm wavelength was used for the excitation of background AF, a 488-nm wavelength was used for the excitation of the fluorescein dye and 2-NBDG molecule, and, finally, a 642-nm wavelength was used for the excitation of the Cy5.5 dye. The resulting multilaser beam is scanned in a spiral pattern by a piezoelectric transducer and is focused onto the target surface by a lens assembly. Fluorescence, or diffuse reflected light, is then collected by a concentric ring of high numerical aperture optical fibers, which surround the single-mode beam delivery fiber and lens assembly. The collected light is separated into four wavelength bands (blue, green, red fluorescence and red reflectance, respectively) by three dichroic beam splitters (FF495-Di03-35x35 495 nm BrightLine® Dichroic Beamsplitter, FF593-Di03-35x35 593 nm BrightLine® Dichroic Beamsplitter, and FF649-Di01-35x35 649 nm BrightLine® Dichroic Beamsplitter, Semrock Inc., Rochester, New York). Unwanted laser light is rejected by passing each wavelength band through a high optical density bandpass

(FF01-470/28-25470/28 BrightLine® Bandpass Filter, or FF01-531/46-25531/46 BrightLine® Bandpass Filter, Semrock Inc.) or long-pass filter (BLP01-647R-25647 nm EdgeBasic™ best-value long-pass edge filter, Semrock Inc.) positioned in front of a high-gain photomultiplier tube (PMT, Hamamatsu R9880U series, Hamamatsu Photonics, Hamamatsu City, Japan). Custom-designed software maps the synchronized detection signals as points in the spiral scan pattern of the single-mode fiber, which are then converted to the two-dimensional pixel position on the RGB digital display—red, green, and blue for fluorescence images and gray scale for reflectance. The resulting images are in spatial registration since all of the excitation lasers simultaneously sample the same target location.

For high-sensitivity fluorescence detection, a new 2.1-mm-outer diameter scope was designed and fabricated for the multispectral SFE system [Fig. 1(a)]. The light collection portion of the scope consists of a concentric ring of six identical 500-micron-diameter multimode plastic optical fibers (Mitsubishi Rayon Co., LTD, Tokyo, Japan). Since the collection numerical aperture remained high (NA = 0.6), it is estimated that the 2.1-mm scope has 20× the collection efficiency of the 1.2-mm-diameter SFE scope due to the larger (20×) collection area of the fibers.[45]

2.2 *SFE Fluorescence Sensitivity Measurement*

Sensitivity of the SFE was defined as the minimum amount of fluorescence measureable by the system. More specifically, the system sensitivity was determined by the lowest concentration of fluorescent dye molecules that can be imaged with an S/N value >2:1 when imaged at video rates (30 Hz). For the sensitivity measurement, the gains and offsets on the PMTs and digital display were kept constant at optimized values. The wide-field imaging angle and distance were also kept constant to guarantee reproducibility of the detection sensitivity measurement.

Two fluorescent dyes for *in vivo* application, sodium fluorescein and cyanine (Cy5.5), were chosen for the sensitivity measurements. Dilutions of sodium fluorescein (Sigma-Aldrich, St. Louis, Missouri) and Cy5.5 N-Hydroxysuccinimide (NHS) ester (Lumiprobe, Hallandale Beach, Florida) were prepared in double distilled water (ddH2O) solutions. For making the dilutions of the Cy5.5 NHS ester, the dye was first dissolved in dimethyl sulfoxide as recommended by the manufacturer, and then serial dilutions were made using ddH2O. Dilutions covered the range from micromolar (μmol/L) to nanomolar (nmol/L) for both dyes, and were kept at pH7.

During the measurement, the SFE 488-nm laser was turned on for detection of sodium fluorescein in the green channel, whereas the SFE 642-nm laser was turned on for the detection of Cy5.5 in the red/NIR channel. All measurements were performed by imaging a 50-μl dye droplet dispensed onto a diffuse, nonfluorescent and flat Teflon surface, with the SFE 2.1-mm scope pointing down perpendicularly to the Teflon surface at a 20-mm distance [Fig. 1(b)]. The imaging performance at video rates (30 Hz) was then evaluated.

As described earlier, high optical density filters (Semrock Inc.) were employed to block light from the excitation laser sources at the PMT detectors. To verify that the background light from the excitation lasers was >10× below the measured fluorescence signals, images were recorded without any dyes placed on the nonfluorescent Teflon surface.

2.3 *Autofluorescence Equivalent Concentration Measurement*

AEC was measured using the preclinical in vivo imaging systems (IVIS) spectrum *in vivo* imaging system (PerkinElmer, Waltham, Massachusetts). Two types of healthy *ex vivo* tissue samples—lower porcine esophagus epithelium and murine brain—were imaged, respectively, with sodium fluorescein and Cy5.5 reference dye solutions placed alongside. The liquid dye solution reference was poured into the flat bottom of an off-the-shelf black phenolic screw-cap (16198-911 VWR, Visalia, California) to a depth of 5 mm.

All animal tissues were prepared under the protocols of the Institute of Animal Care and Use Committee approval or Standard Operating Procedure for porcine tissue from abattoirs by the University of Washington.

Brains were freshly harvested from a group ($n = 5$) of wild-type nude (nu/nu) mice (same sex, age, and weight). Meanwhile, porcine esophagus tissue of the same age and weight group ($n = 5$) were obtained from a certified abattoir. The lower 1/3 of the esophagus was cut open and placed flat on a glass surface (chamber slide, Fisher Scientific, Hampton, New Hampshire) with the epithelium layer facing up for imaging.

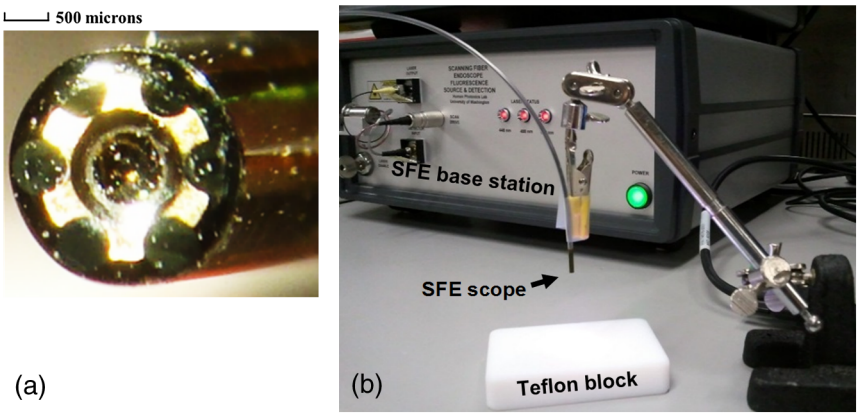

Fig. 1 (a) The end-face of the new 2.1-mm scanning fiber endoscope with six 500-micron optical fibers held in a brass ring surrounding the distal lens for the scanned illumination. (b) Experimental setup for the fluorescence sensitivity measurement.

To get a full assessment of the AF excitation-emission profile of the tissues, a wide range of excitation (430 to 745 nm) and emission (500 to 840 nm) filter combinations were employed with the IVIS spectrum (Perkin-Elmer, Norwalk, Connecticut) fluorescence imaging system. During the imaging process, system settings, such as exposure time, f number, and field of view, were kept constant. The IVIS quantitative unit of the fluorescence emission intensity is defined as the number of photons per second per centimeter squared per steradian ($p/s/cm^2/sr$). Quantitative fluorescence emission intensities were analyzed off-line on the recorded images and averaged across the same tissue type group.

2.4 *Orthotopic Mouse Brain Tumor Models*

Orthotopic xenograft models were created by implanting 1×10^5 tumor cells in suspension through a 1-mm burr hole in the right parietal bone above the cerebellum ~2 mm posterior to the bregma and 3 mm beneath the dura. This study used pediatric patient derived medulloblastoma model MED-211FH. Tumor cells came from donor mice bearing symptomatic intracranial tumors and were transplanted directly into male and female the NOD scid gamma (NSG) mice. Tumors were allowed to grow until mice presented with clinical symptoms of tumor burden, such as head tilt and cranial bulge (35 days for the MED-211FH model). At the first onset of clinical tumor burden, mice were given 100-μl intravenous tail-vein injections of 20 μM chlorotoxin conjugated to Cy5.5 (Tumor Paint™, Blaze Biosciences, Seattle, Washington) and imaged in the NIR spectrum as previously described.[8] It was reported in previous publications[8,46] that specific binding of Tumor Paint™ to cancer cells is facilitated by matrix metalloproteinase-2. Brains were harvested after euthanasia via CO_2 inhalations, imaged, and then fixed in 10% neutral buffered formalin. All mice were maintained in accordance with the National Institute of Health (NIH) Guide for the Care and Use of Experimental Animals with approval from the Fred Hutchinson Cancer Research Center Institutional Animal Care and Use Committee (IR#1457).

2.5 *Multispectral Molecular Imaging of Ex Vivo Mice Brain*

SFE fluorescence molecular imaging was performed on the *ex vivo* mice brain within 1 h after they were harvested. Images of the same brain using the IVIS spectrum system immediately after harvesting were used as a reference. Images of the bulk fluorescently labeled tumor margin from both imaging systems were compared. To guarantee a fair comparison of molecular probe distribution, experimental settings, such as the excitation and emission wavelength on both imaging systems, as well as imaging angle and exposure time, were kept as closely matched as possible. Three types of control brains—wild-type mice alone, wild-type mice with Tumor Paint™ injection, and MED-211FH mice with no injection—were also imaged. After the imagings were performed, brains were fixed in 10% neutral buffered formalin; then tissue blocks were embedded in paraffin, cut into 4-μm sections, and stained with hematoxylin and eosin (H&E) using standard methods. Slides were scanned on an AperioScanScope AT (Leica Biosystems, Buffalo Grove, Illinois).

2.6 *Barrett's Esophagus Tissue Phantom Model*

Details of the biological phantom design and development can be found in Ref. 47. Briefly, bovine collagen (Sigma Aldrich) was digested using collagenase (Life Technologies, Carlsbad, California) and reconstituted into a solid gel to serve as the AF background. Rat tail collagen gels (Life Technologies) were seeded with CP-D (American Type Culture Collection, Manassas, Virginia), a high-grade dysplasia (HGD) Barrett's esophagus (BE) cell line. Cultures were fixed in methanol. Overexpression of epidermal growth factor receptor (EGFR), receptor tyrosine-protein kinase erbB-2 (ERBB2), and MET or MNNG HOS transforming gene (C-MET) were identified through indirect immunofluorescence (IF) staining. IF staining was performed using goat Alexa Fluor 488 (Life Technologies) conjugated antibodies to target anti-ERBB2, anti-EGFR, and anti-C-MET. The seeded gels were laid upon the solid collagen background for imaging.

2.7 *Multispectral Molecular Endoscopic Imaging with AF Mitigation*

Multispectral SFE imaging of the BE tissue phantom was performed with an AF mitigation algorithm running in real time to achieve a high T/B as well as to eliminate bleed-through specular reflections. A graphical illustration of the algorithm is shown in Fig. 2. Since higher laser powers were desired for the *in vitro* testing, the multispectral fluorescence was excited using a Coherent OBIS Galaxy system with fiber pigtail (FP) lasers[48] at 445, 488, and 642 nm, which proved to have plug-and-play simplicity across the spectrum with the single-mode optical fiber coupling to the SFE.[49] The implementation employs simultaneous excitation by two closely spaced laser wavelengths: 488 nm as the targeting beam and 445 nm as the AF reference beam. Fluorescence in the blue channel is dedicated to the AF emission, whereas the green channel contains a mixture of fluorescein and AF background emission. Based on the AF signal from the concurrent blue channel and a precalibrated ratio, the AF component in the green channel background AF is subtracted in real time within the SFE operating system software. As a result, an increase in fluorescein T/B is achieved.

3 Results

3.1 *Multispectral Scanning Fiber Endoscope System*

The new multispectral SFE [shown in Figs. 3(a), 3(b), and 3(c)] was custom-fabricated for the purpose of fluorescence molecular endoscopy. Under standard operating conditions, the video imaging system has a 30-Hz refresh rate, with an 80-deg field of view, 50-microns image resolution, and a depth of focus from 2 to 50 mm. Three fluorescence channels and one reflectance channel are simultaneously processed to create spatially coregistered blue, green, and red fluorescence images and a gray-scale reflectance background image. All of the images are inherently coincident by virtue of the simultaneous laser scanning and light collection design of SFE. Concurrently, wide-filed and high-resolution imaging was demonstrated on all channels for the multispectral SFE, with an intraoperative navigation feature derived from the gray-scale reflectance background. The system also operates with quantitative fluorescence imaging to guide biopsies based on a previously published distance compensation algorithm.[50]

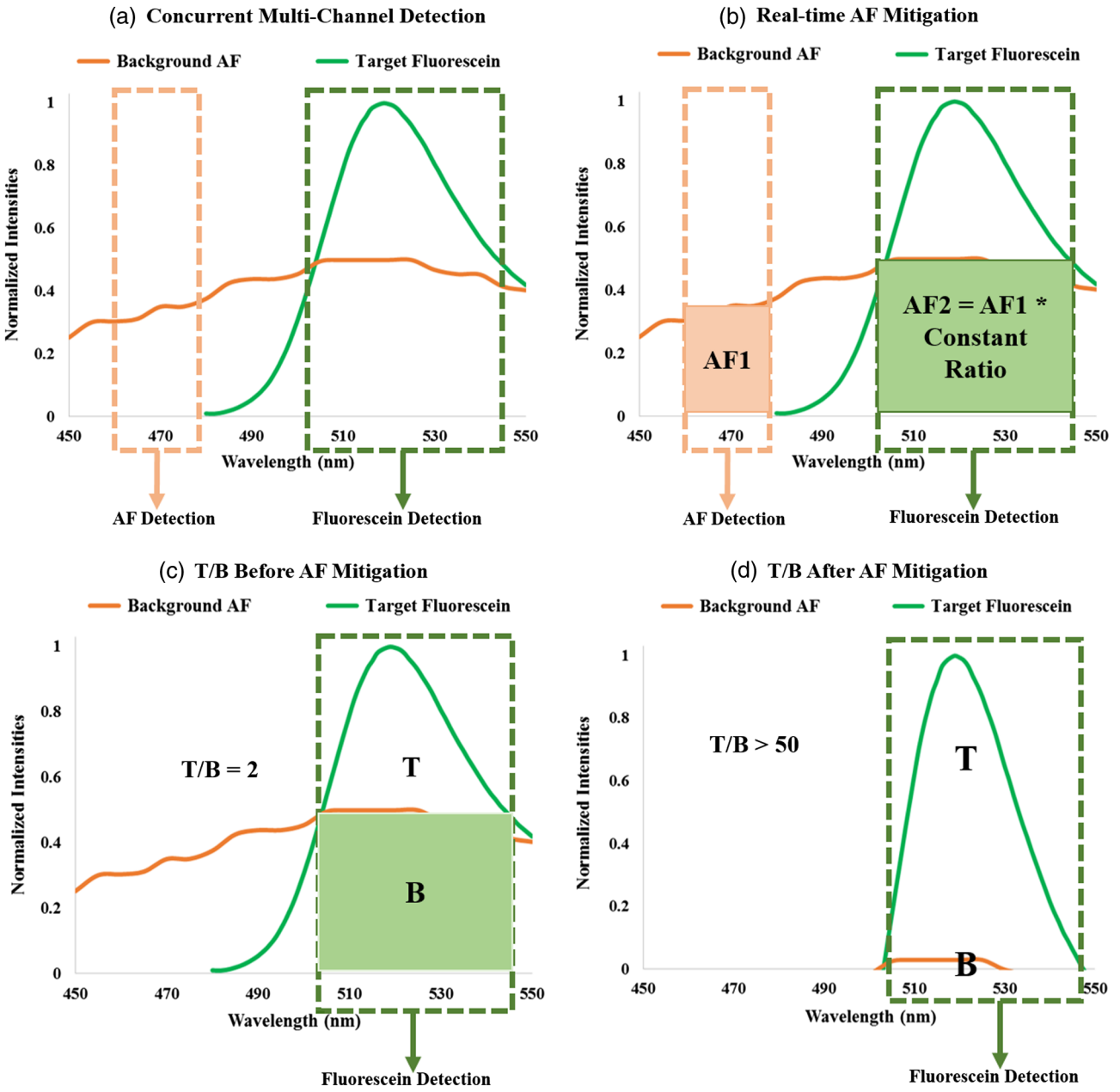

Fig. 2 Graphical illustration of the real-time autofluorescence (AF) mitigation algorithm on the multispectral SFE system for fluorescein fluorescence imaging.

3.2 *Imaging Device Detection Sensitivity*

The detection sensitivity of the SFE was evaluated on a series of low-volume (50 μL) and low-concentration (nanomolar to micromolar) fluorophore dilutions. In the current study, sodium fluorescein and Cy5.5 dyes were chosen for the sensitivity test, since they were to be used in the following *ex vivo* or *in vitro* image applications. SFE output powers were <3 mW for each channel and were maintained constant for the experiments.

The multispectral SFE detection sensitivity limit was 5 nM for the sodium fluorescein dye and 10 nM for the Cy5.5 dye at video rates with an S/N of 2:1. The SFE detection channels' linearity was previously demonstrated over the 0- to 100-μM range;[51] the same method was also used here by plotting the dye concentration versus the image intensity relationship to confirm the detection channel linearity over the 0- to 100-nM range (Fig. 4).

3.3 *Autofluorescence Equivalent Concentration—the Brain and the Esophagus*

AEC was determined in a side-by-side comparison of the fluorescence intensity from a sodium fluorescein or Cy5.5 dye standard with the intensity from the fresh *ex vivo* brain and esophagus tissue sample. Quantitative fluorescence imaging was performed with the IVIS spectrum system and the recorded images were analyzed off-line. To avoid photodegradation, all the samples were kept in a dark container before moving them into the IVIS's sample chamber, and the images were

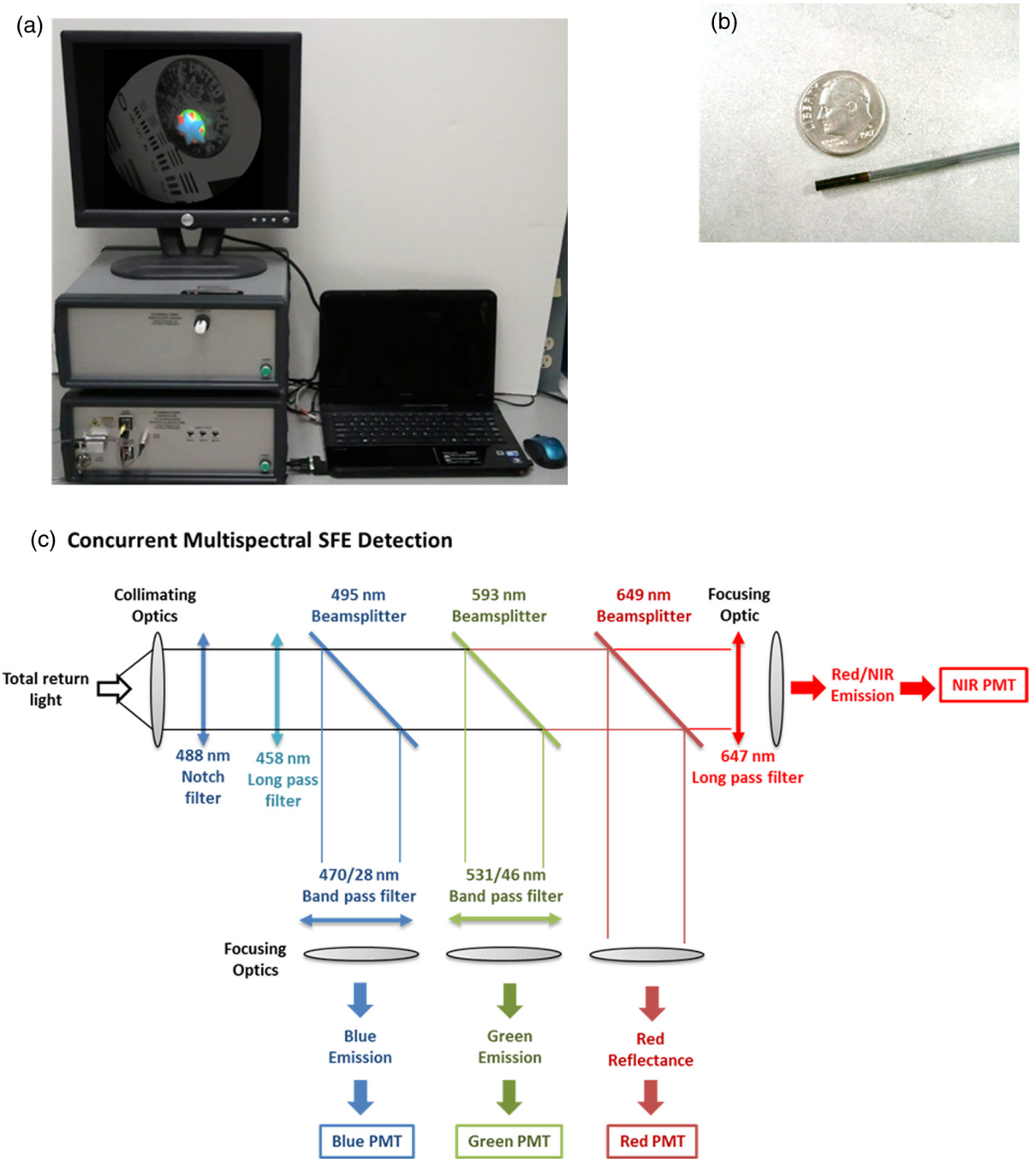

Fig. 3 Real-time, high-sensitive, and concurrent multispectral fluorescence SFE system with a 2.1-mm endoscope. (a) System in operation. (b) Ultrathin endoscope. (c) Concurrent multichannel fluorescence separation and detections.

taken within 10 s after the samples were exposed to room light. No dye loss from the IVIS imaging light exposure (exposure time: 1 s) was observed.

For defining the AEC of sodium fluorescein dye in the esophagus epithelium and brain tissue, the IVIS bandpass excitation filter at $460/(\pm 15)$ nm was chosen as a close match to the SFE's 488 (fluorescein) excitation laser, and the IVIS $520/(\pm 10)$ nm bandpass fluorescence detection filter was selected as the corresponding emssion wavelength. Likewise, the AEC of Cy5.5 dye was defined by imaging the same esophgeal and brain tissue under the IVIS excitation filter at $640/(\pm 15)$ nm corresponding to the SFE's 642-nm excitation laser, and the IVIS emission filter at $700/(\pm 10)$ nm was used to collect the fluorescence signal.

As shown in Fig. 5, at $460/(\pm 15)$ nm excitation, the 10 nM concentration of fluorescein was found to be equivalent to the esophagus epithelium tissue group in fluorescence/AF emission intensity [Fig. 5(a)], whereas the AF emission intensity from the brain tissue group was 5× lower compared to the same sodium fluorescein sample [Fig. 5(b)]. Therefore, at $460/(\pm 15)$ nm excitation, the sodium fluorescein AEC in porcine esophagus was 10 and 2 nM for mice brain. Meanwhile, at $640/(\pm 15)$ nm excitation, the AF from the esophagus was 5× lower compared to the emission from a 10-nM Cy5.5 dye, and the brain AF

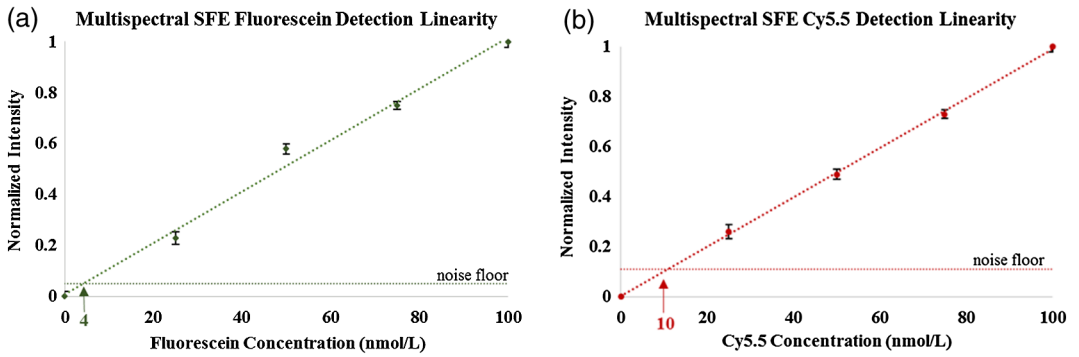

Fig. 4 Dye concentrations (0 to 100 nmol/L) are plotted as a function of the detected fluorescence signals in the SFE images. Each data point was an average of $n = 5$, and the error bars represent the variability in the fluorescence signal intensity measurement. The linearity of the sodium fluorescein fluorescence in the SFE's green channel is presented in (a), whereas in (b) the linearity of the Cy5.5 fluorescence in the SFE's red detection channel is shown.

signal was 1/5 the emission signal from the same Cy5.5 dye standard. Therefore, at $640/(\pm 15)$ nm excitation, the AEC for porcine esophagus epithelium tissue was 2 nM for Cy5.5 and 1 nM for mice brain tissue.

3.4 *Quantitative Autofluorescence Analysis of Ex Vivo Esophagus and Brain*

For quantitative understanding and comparison of the AF emission pattern across the visible to infrared spectrum, tissue AF of the esophagus and brain tissue were captured separately with all of the available IVIS spectrum's excitation-emission filter combinations. The relative AF amplitudes for porcine esophagus epithelium and mouse brain, respectively, are plotted in Figs. 6(a) and 6(b) under excitation from 430 to 675 nm and an emission across a range of 500 to 820 nm. As shown in the graphs, the AF emission intensity for both tissue types peaked at ~500 to 520 nm, with maximum excitation at the shorter wavelengths (430 to 465 nm). For a fixed excitation, the AF emission signal declined when moving from short to longer wavelengths and reduced by 10× when moving beyond 800 nm. Meanwhile, AF emission also decreased when the excitation wavelength shifted from 430 nm to longer wavelengths. However, even with the intensity decline, the AF emission signal remained detectable (>10% peak intensity) in the 600- to 800-nm range from both tissue types.

Figure 7 represents the AF emission spectral profiles from the esophagus [Fig. 7(a)] and the brain [Fig. 7(b)] for different excitation wavelengths. Each excitation spectral profile was derived from the IVIS AF signal intensities with a scaling factor. This factor is the ratio of the maximum AF intensity measured at 430 nm divided by the maximum AF intensity of the particular excitation data series being plotted. The scaling factors are also shown on the graph alongside the assigned spectral profiles.

A red-shift phenomenon was observed in all of the normalized AF spectral profiles plotted in Fig. 7. Specifically, each emission profile/shape remained nearly the same, whereas the peak spectral wavelength was red-shifted from 500 to 750 nm as the excitation wavelength changed from 430 to 675 nm. Interestingly, both tissue types exhibited similar emission profiles and peak spectral intensities under 430- and 465-nm excitation.

The scaling factors indicated that the emission intensity decreased as the excitation wavelength changed from visible to NIR, but the AF signal was still detectable in the NIR range. For the esophagus epithelium tissue, the AF signal dropped by a factor of 5× at 500-nm excitation compared to the peak excitation at 430 nm and continued to decrease by a factor of 10× at 550-nm excitation, and eventually by 34× at 675-nm excitation. However, the AF decline for the brain tissue was much slower, with only a 4× decrease at 675-nm excitation compared to the peak excitation at 430 nm.

3.5 *Molecular Imaging of Brain Tumor Detection*

Highly sensitive SFE molecular imaging was demonstrated on *ex vivo* mice brain tissue with xenograft human-derived tumor. Details regarding the Tumor Paint™ molecular imaging probe can be found in previous publications.[8] Eight hours following tail vein injection of 0.1 mL 20 μM chlorotoxin (CTX): Cy5.5 conjugate, a side-by-side comparison between IVIS and SFE quantitative molecular imagings was conducted.

As shown in Figs. 8(a) and 8(b), there was no observation of specific Tumor Paint (TP) accumulation using the IVIS and SFE imaging systems for the wild-type mice with a TP injection. On the other hand, in Fig. 8(c), for the xenograft tumor mice with a TP injection, a mass accumulation of the molecular target was observed, and the resultant tumor margin was confirmed from the IVIS, SFE, and H&E images on all the tumor mice brains. Images from different devices (IVIS and SFE) or a different methodology (imaging or H&E pathology stain) consistently indicated that this type of tumor xenograft demonstrated a diffuse pattern and is located beneath the tissue surface. Isolated red spots in the SFE images correspond to specular reflections from the tissue surface.

Quantitative image analysis showed that T/B for SFE real-time imaging was on average 2.3, whereas T/B for IVIS was ~2.1. Images from the wild-type mice without TP injection suggested that the background signal was mostly contributed by tissue AF.

3.6 *Real-Time AF and Specular Reflection Mitigation on a Tissue Phantom*

A real-time AF mitigation algorithm was implemented in the software operating system of the multispectral SFE. To demonstrate the performance of the algorithm, a tissue phantom was designed and constructed to simulate the three-dimensional anatomical structure of the GI tract. Specifically, the tissue phantom

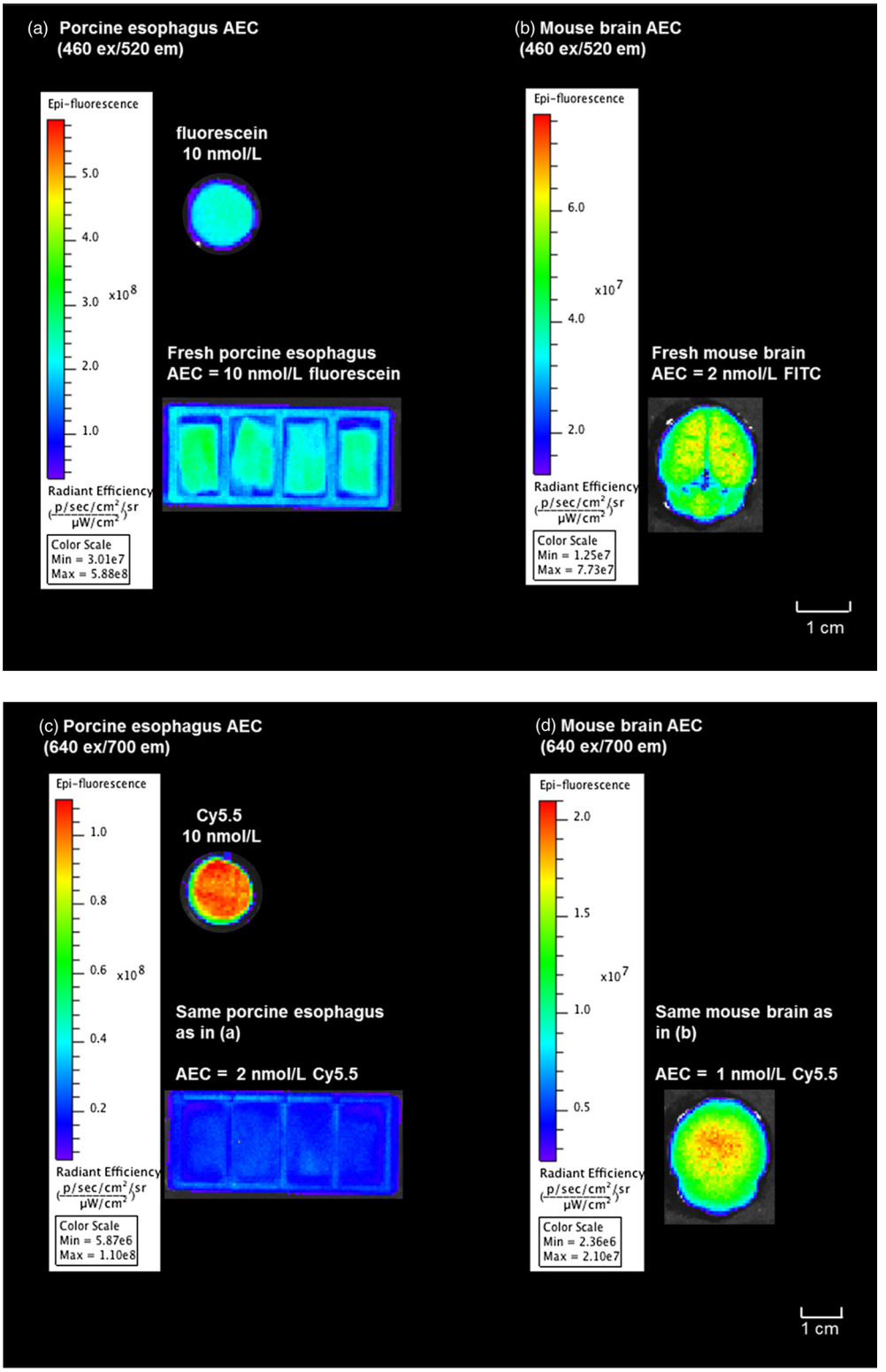

Fig. 5 Autofluorescence equivalent concentration evaluation using the IVIS spectrum. (a) and (b) Side-by-side quantitative fluorescence intensity comparison of 10-nM fluorescein sodium solution, healthy porcine esophagus tissue, and wild mice brain under the IVIS spectrum imaging. Excitation filter $460/(\pm 15)$ nm was used, and emission was gathered by the $520/(\pm 10)$ nm filter. (c) and (d) Side-by-side comparison with exactly same *ex vivo* tissue samples, and 10-nM Cy5.5 solution under IVIS. In this case, $640/(\pm 15)$ nm was used for the excitation and $700/(\pm 10)$ for the emission. Settings on the IVIS spectrum (e.g., exposure time, *f* number, field of view, etc.) were kept constant. The quantitative unit of the fluorescence emission intensity is defined as photons per second per centimeter squared per steradian ($p/s/cm^2/sr$). Since this is an absolute quantification unit, quantified fluorescence intensities can be compared using the same absoute quantification unit.

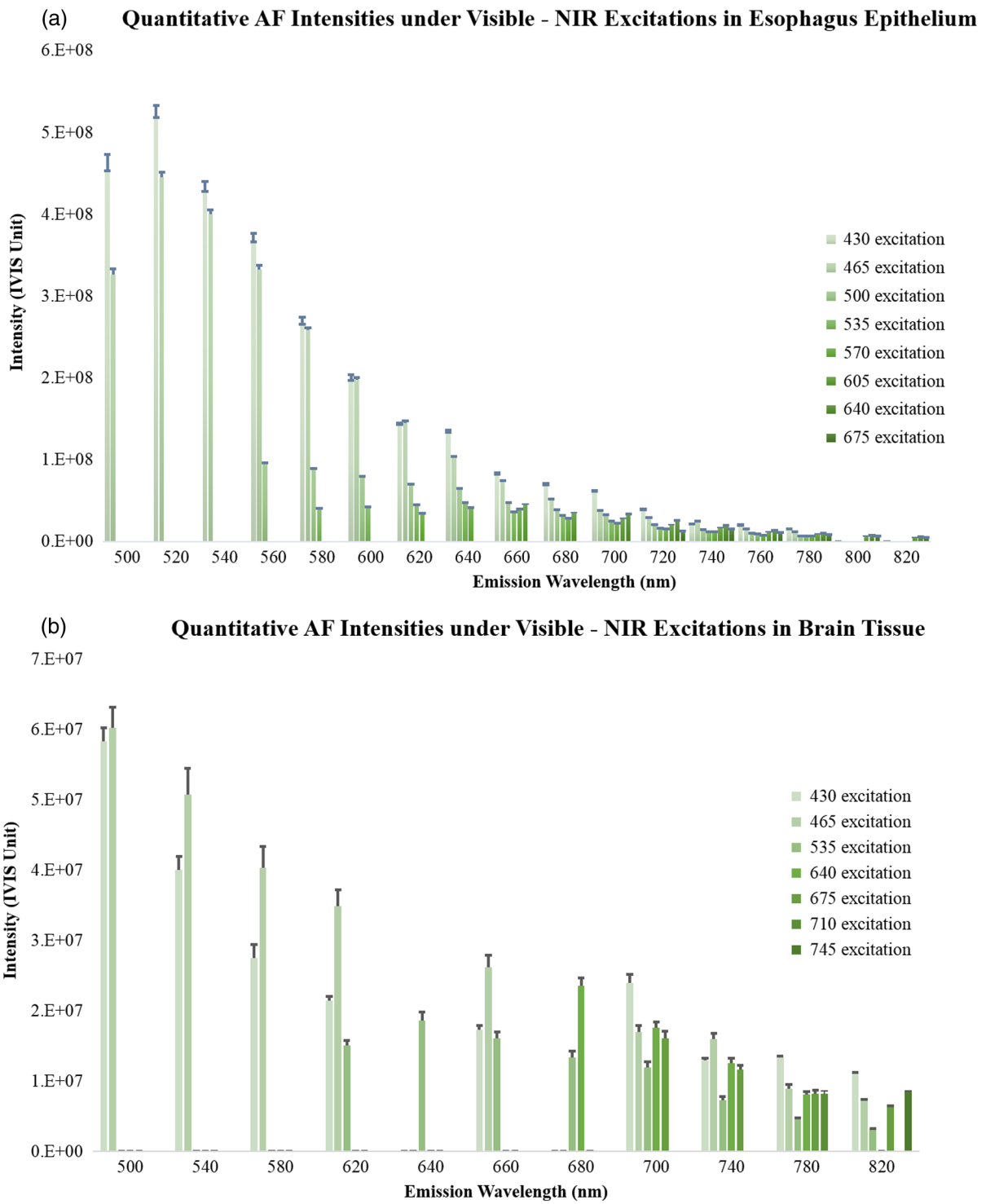

Fig. 6 Quantitative AF analysis of esophagus epithelium and brain tissue under a wide range of excitations from 430 to 675 nm.

featured a mucosal BE with a monolayer HGD and esophageal adenocarcinoma cell, as well as a submucosal collagen matrix, which is known to be a major contributor to the background AF signal.[52] fluorescein isothiocyanate (FITC) conjugated molecular probes targeting cancer-specific proteomic biomarkers (EGFR, HER2, and CypA) were applied to the phantom, as well as metabolic molecular probe 2-NBDG, respectively, to demonstrate the AF and specular reflection mitigation algorithm.

As described previously, 445- and 488-nm laser beams were simultaneously launched into the SFE scanning fiber as excitation light sources, each producing 7-mW outputs on the tissue. The 445-nm excitation served as the reference beam to excite the tissue AF, whereas the 488-nm excitation targeted the fluorescein molecular markers. Traditionally, in the target detection channel, the fluorescence signal would contain an unavoidable AF background signal which reduces the T/B. However, with

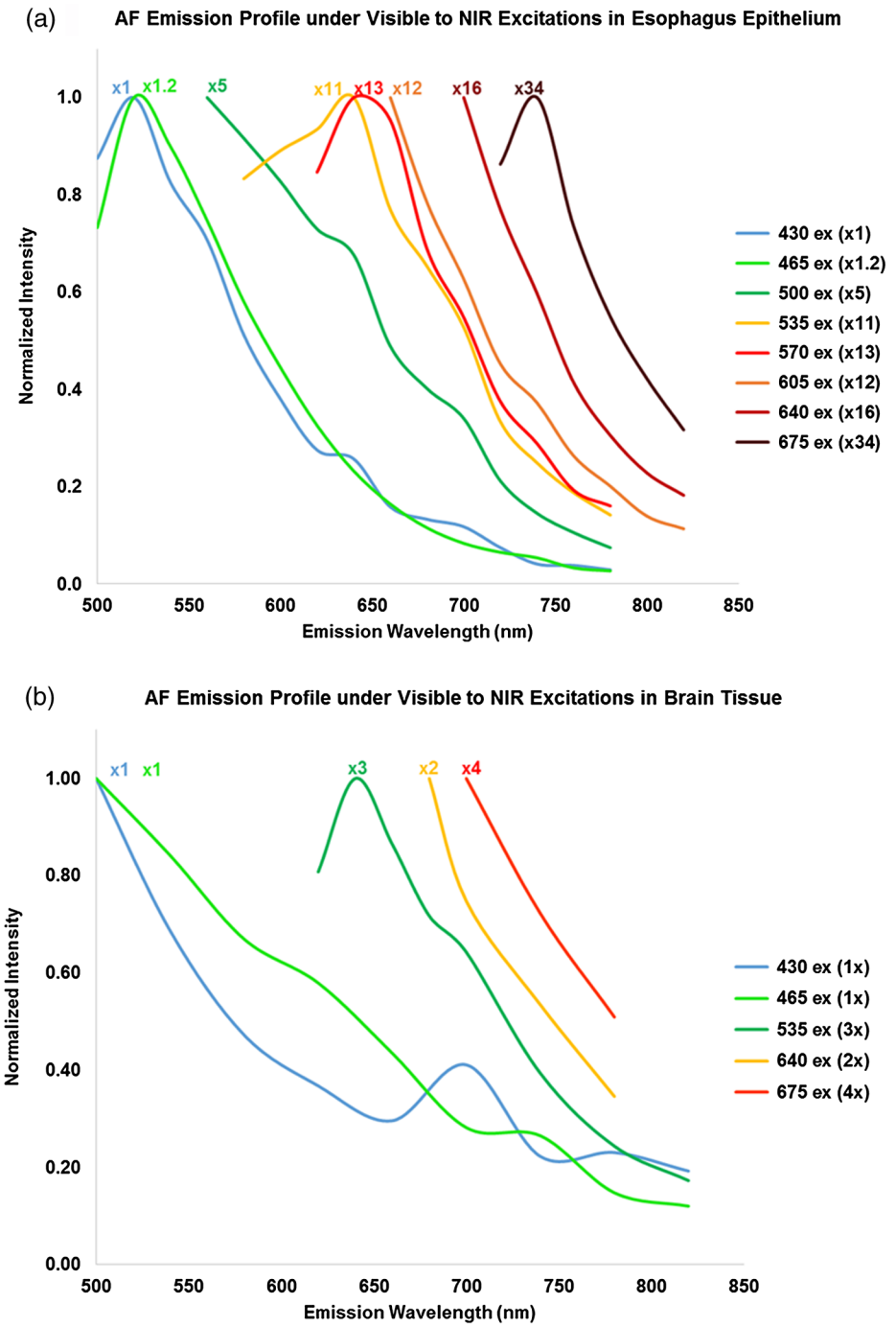

Fig. 7 Autofluorescence excitation and emission spectral characteristics of porcine esophagus and murine brain tissue.

the algorithm running in real time, the AF excited via the 445-nm excitation and received in the SFE blue detection channel is proportional to the quantity of background AF signal in the concurrent target fluorescein/green channel. Therefore, AF mitigation can be achieved by subtracting the background AF signal in the green channel by a predetermined factor of the concurrent AF signal in the blue channel. The algorithm runs automatically on a pixel-by-pixel basis at high resolution (50 microns) and at real-time video rates (30 Hz).

Furthermore, an additional benefit of the AF mitigation algorithm was realized with multiple fluorescence imaging channels. Specular bleed-through artifacts in the fluorescein/green channel were also subtracted based on the signals from the AF/blue channel at the same pixel location, as all the detection channels of the SFE system are spatially coregistered.

The results shown in Fig. 9(b) demonstrated the significant improvement of T/B and elimination of specular reflection after applying the AF mitigation algorithm. Specifically, the T/B ratio increased from 2.1 to 117.7—a 56-fold improvement, and the specular reflection from Fig. 9(a) was removed, resulting in a clean and clear delineation of the targeted disease region. The same algorithm was also applied to a lumen-shaped tissue

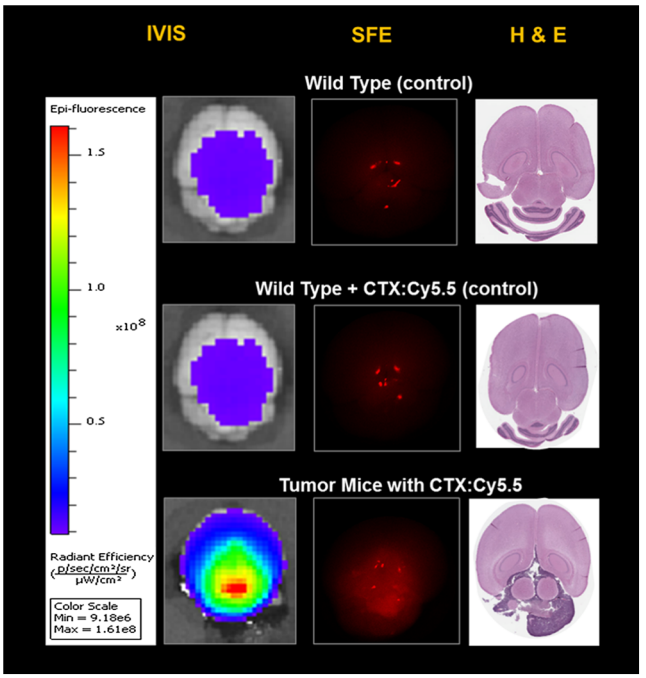

Fig. 8 Tumor paint (CTX:Cy5.5) imaging of mouse xenograft tumor.

phantom with an AF background and a 2-NBDG target (Fig. 10). Significant T/B 44-fold enhancement from 2.1 to 88.0 was also observed.

4 Discussion

High sensitivity at nanomolar fluorophore levels is needed for a viable fluorescence molecular endoscopic imaging device to detect disease-associated cellular biomarkers and guide interventions. Apart from achieving a high S/N as an electronic device, the success of a clinically viable molecular diagnostic imaging system also depends on the *in vivo* image contrast ratio (T/B). However, a low T/B ($\leq$3) is often reported and is caused by a combination of confounding factors, including the abundant tissue background AF.[8,13–16,36,37] Sometimes the background AF signal can be as high as the target signal. It blocks out diagnostic information and reduces the net sensitivity of the molecular probe imaging.

It is a general concern that tissue AF is a major limiting factor for achieving high contrast ratio in exogenous fluorophore probe imaging. Although quantitative dilutions of the target fluorophore are routinely used for evaluating an imaging device's detection capability, the quantitative signal strength of the background AF and its amplitude compared to the target signal are often unaddressed. The omission of this AF interference impedes the evaluation of the imaging device's *in vivo* detection capability. In the present study, we established AEC as an additional requirement for fluorescence molecular imaging device evaluation and performed the AEC measurement of targeted tissues with references to a quantitative fluorescence *in vivo* imaging instrument—the IVIS spectrum. The AEC method enables researchers to prepare portable calibration standards without the need for complex radiometric measurement systems.

We propose and demonstrate herein a two-step method for evaluating a fluorescence molecular imaging device's detection sensitivity. The evaluation method is based on two major factors: (1) determine the S/N of the device itself *in vitro* using low concentrations of fluorophore dye probes, and (2) evaluate the actual T/B in the presence of tissue background AF. Here, the AF signal is quantitatively assessed and transferred into the AEC of standardized fluorophore solutions. The fluorophore reference concentrations are determined in a side-by-side comparison with the quantitative tissue AF signal. The fluorophore concentration that quantitatively matches the AF background (Fig. 5) is then selected as the portable AEC standard.

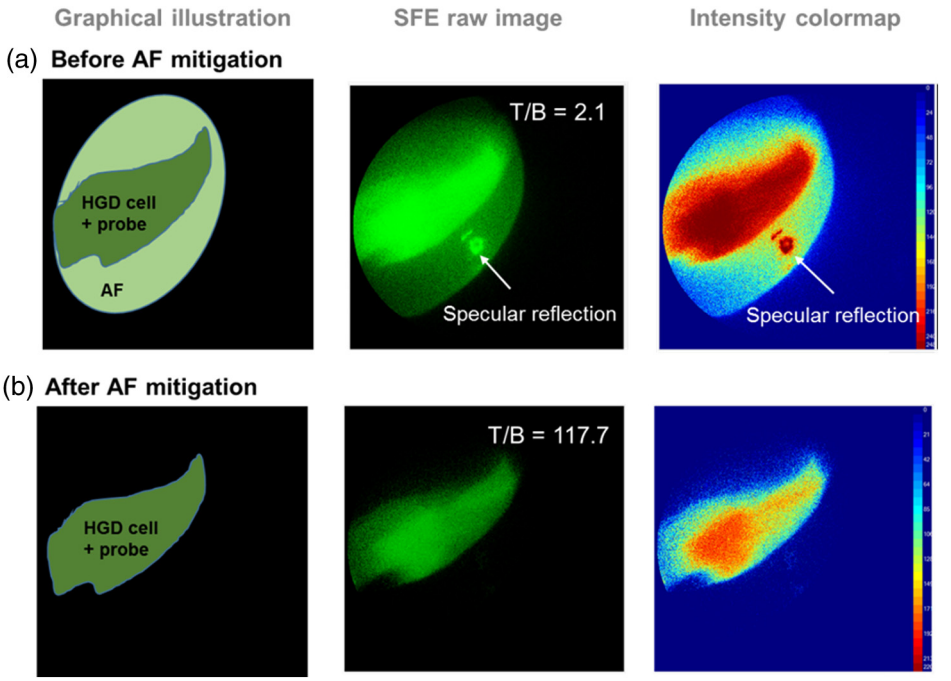

Fig. 9 Real-time AF and specular reflection mitigation on a flat tissue phantom with molecular specific labeling using fluorescein isocyanine conjugated probes.

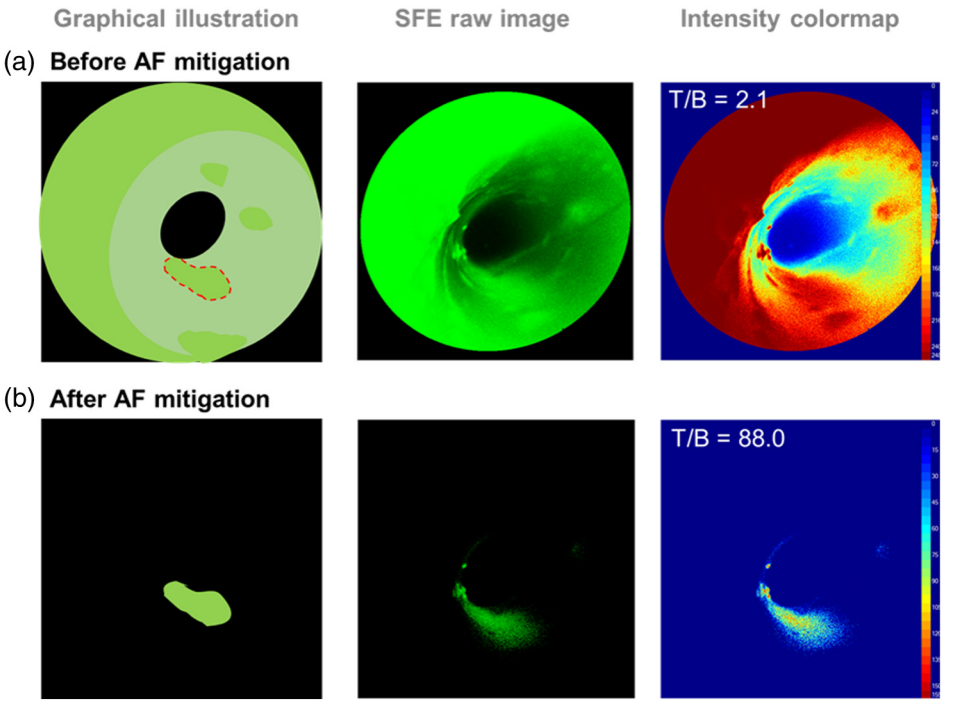

Fig. 10 Real-time AF mitigation on a lumen-shaped tissue phantom with a 2-(N-(7-nitrobenz-2-oxa-1,3-diazol-4-yl)amino)-2-deoxyglucose target.

The quantitative AF measured from healthy esophagus and brain tissue also revealed the heterogeneity of AF signals among different animal species and tissue/organ types. For instance, as shown in Fig. 11(a), under blue (460 ± 15 nm) excitation, the AF emission from the esophagus is significantly higher than that of the brain; on the other hand, under NIR (640 ± 15 nm) excitation, the difference between the background AF signals was much less significant [Fig. 11(b)]. Also represented in the scaling factors in Figs. 7(a) and 7(b), from blue to NIR excitations, the decline of the peak esophagus AF signal is much faster than the decline of the peak brain AF. This quantitative assessment led to the estimate of AF background in brain tissue using probes containing red/NIR dyes. In fact, background AF was recognized in molecular endoscopic imaging of the xenograft mice tumor model using the Cy5.5 TP probe (Fig. 8, wild-type control mice, 640 ± 15 nm excitation). This result is in agreement with previous publications that background AF signals were present and detectable even beyond the visible spectrum.[46]

Flavins, in particular flavin adenine dinucleotide (FAD), are the likely major contributors to the murine brain tissue AF excited at 435 and 465 nm [Fig. 6(b)].[53] The reduction in AF for excitation at longer wavelengths follows a sharp decrease in FAD absorption beyond 500 nm.[54–56] Nicotinamide adenine dinucleotide$^+$, although present in the brain tissue,[53] has very little absorption beyond 400 nm[57,58] and is, therefore, not a significant contributor to the measured murine AF. In the current study, the short time between harvesting the brain tissue and IVIS data collection (<= 30 min) and repeatable AF measurement results are consistent with minimal redox changes to the FAD.

Any molecular imaging devices' contrast ratio will be limited to the AF background unless the device can mitigate the unwanted AF signal. To achieve a high *in vivo* imaging T/B ratio, we implemented a real-time AF mitigation algorithm in the operating system software of the multispectral SFE and demonstrated a T/B exceeding 80 using two different phantoms. This represents more than a 40-fold increase from a T/B of 2.1 without AF mitigation in the visible spectrum. These real-time imaging results were obtained with a tissue phantom featuring a collagen submucosal background and molecular targeting of mucosal early cancerous cells with 488 nm excitation.

In addition, the AF mitigation algorithm can also serve as a simultaneous specular reflection elimination algorithm. We demonstrated the elimination of false positive imaging artifacts caused by tissue specular reflections. Specular reflections are unavoidable when viewing glossy tissue surfaces, such as the lung, oral and GI mucosa, blood vessels, bladder, etc., even with well-selected high optical density (=10) laser rejection filters. The bleed through signal creates false positive information and leads to less specific results in molecular target identification. Compared to other approaches to mitigate bleed-through specular reflections such as installing polarization filters or constantly moving the angle of the endoscope to adjust light incident angles, the current approach is more convenient, economical, and practical for clinical applications.

AF mitigation algorithms have also been reported and implemented in a single frame camera imaging system,[35,59] and a T/B improvement of 23-fold was reported in Ref. 35. However, real-time AF mitigation on an endoscopic device has not been previously reported. The principle of the current AF mitigation algorithm works by simultaneously launching a reference excitation laser together with the fluorophore excitation laser and obtaining the respective emission signals in concurrent but separate detection channels (Fig. 3). Mitigation of the background AF signal is realized by subtracting the target signal (fluorescein + AF2) from the reference signal (AF1) multiplied with a precalibrated ratio, at a pixel-by-pixel resolution.

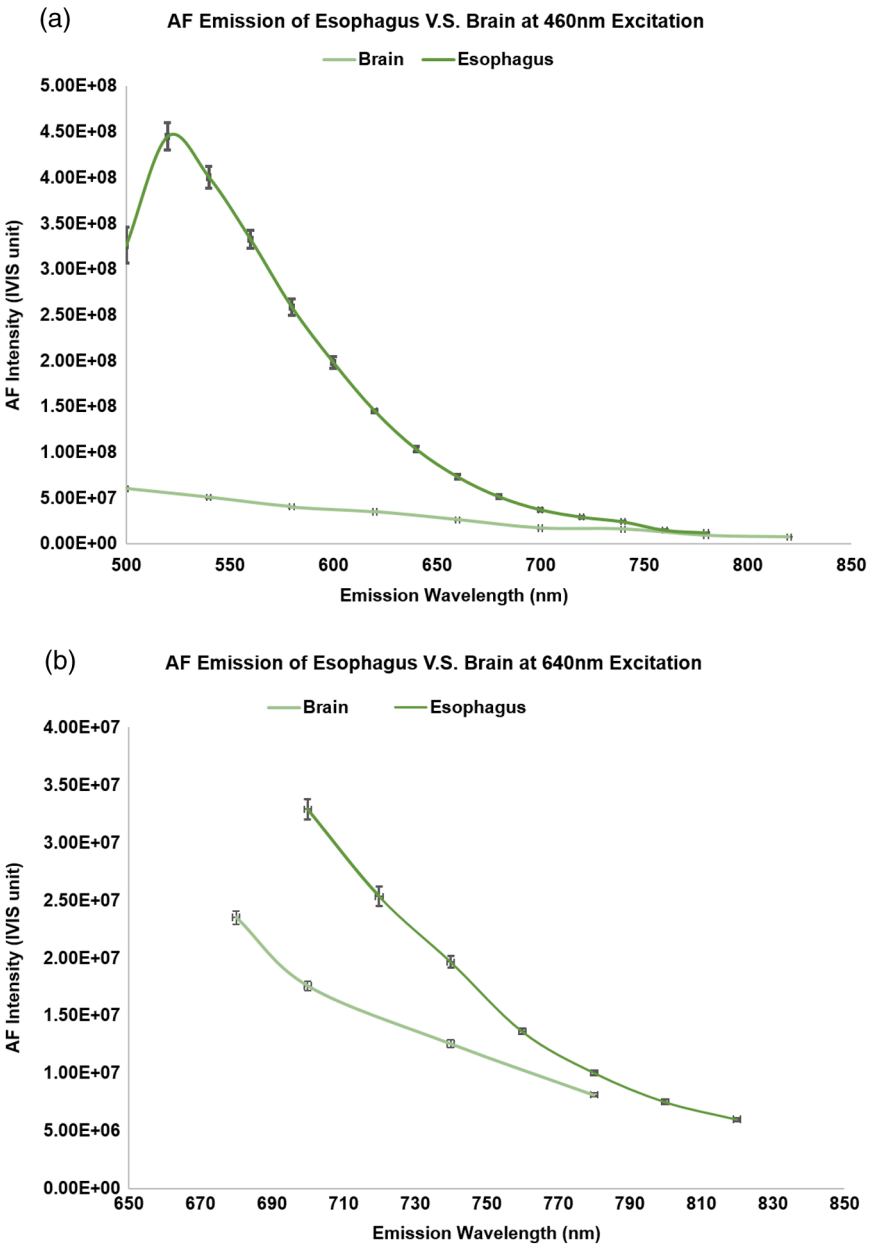

Fig. 11 AF comparison of the esophagus versus the brain (at 460-nm excitation and 640-nm excitation).

The basis for this type of AF mitigation is the assumption that the AF emission spectral profiles were nearly identical for both 448- and 488-nm excitations. In the present study, we validated this assumption and showed that for both esophagus and brain, the AF emission profiles from the two separate excitation sources (430 ± 15 and 460 ± 15 nm) were nearly identical and even their emission intensities were very similar (Fig. 12). Further assessment also showed that the AF emission spectra profiles from blue to NIR were nearly identical for both of the tissue types studied, indicating that the AF mitigation algorithm can be used for not only two close-by channels (e.g., the 448- and 488-nm excitation and corresponding fluorescence detection channels in Fig. 2), but also a variety of other channels with the appropriate precalibrated ratio.

Furthermore, the current study demonstrated many clinically viable features for the newly developed multispectral SFE applied to fluorescence molecular imaging. First of all, the endoscope's small size and flexibility with high resolution and high detection sensitivity will allow for many applications, including the fluorescence molecular diagnostics in small ducts and tissue cavities, such as the peripheral lung, bile duct, and vascular system. Meanwhile, transnasal or keyhole brain surgeries may be realized with SFE in the near future. Second, concurrent laser excitation with separate detection channels can allow for customized designs for a variety of fluorophore conjugate probe combinations. Finally, high T/B quantitative fluorescence imaging with real-time AF and specular reflection mitigation will serve to increase the sensitivity and specificity of molecular imaging systems. Having an artifact-free, high-contrast multimodal image opens the door to new medical applications, such as applying machine vision on an endoscopic device for computer-assisted diagnosis at the point of care performed

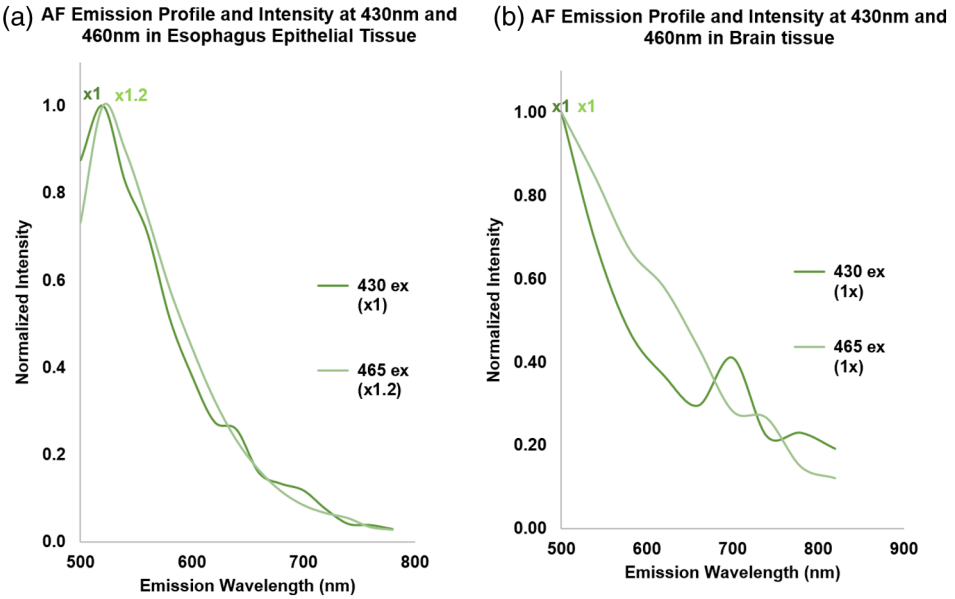

Fig. 12 AF mitigation rationale and emission profile consistency under two different excitation lasers.

by nonexperts and automating tedious therapeutic procedures guided by experts.

The motivation to develop the current real-time AF and specular reflection mitigation algorithm was for surface tissue imaging of topically applied molecular probes in order to red-flag and guide the biopsy of early cancerous lesions.[21,27,60,61] In addition, quantitative assessment of the background AF as well as the mitigation algorithm can also be extended to apply to more subsurface tissue imaging during fluorescence-guided surgery.[8,15,27] During subsurface tissue imaging, other confounding factors, such as scattering and hemoglobin absorption, will be considered. However, applications using two adjacent excitation laser wavelengths, such as 448 and 488 nm demonstrated in this study, may be robust enough to allow for both surface and subsurface tissue imaging since their scattering and hemoglobin absorption profiles are quite similar.[62]

The excitation and emission features for sodium fluorescein and 2-NBDG used in this study lie within the visible range, where the background AF is comparatively higher than in the NIR range. An easy approach to avoid background AF would be to simply use dyes that emit at NIR wavelengths. However, concerns about nonspecific binding exhibited by many NIR dyes, such as ICG and most cyanine dyes, have been addressed.[23,27] Because these dyes are not neutrally charged, they are susceptible to forming nonspecific bonds which increase the fluorescence background and, thus, reduce the T/B ratio.[22,63] Moreover, recent studies have also shown that, even for applications of conjugated NIR molecular probes, background AF still remains a major limiting factor to achieving a high contrast ratio.[36,37] Therefore, in addition to the advancement of NIR fluorescent dyes,[23,63] approaches for background AF mitigation are still in need for improved T/B imaging in NIR molecular probe imaging.

In the meantime, the inherent benefits of fluorescein-based molecular probes can now be realized, thanks to the real-time AF mitigation algorithm combined with a multichannel laser-based flexible endoscope. In addition to >90% quantum yield, good water solubility, high molar absorptivity, neutral charge, and, thus, low nonspecific binding to tissue, the FDA-approved and low-cost fluorescein dye also possesses the advantages of overlapping the widely used 488-nm excitation laser and sensitive visible wavelength of photodetectors. Fluorescein derivatives are easily conjugated to antibodies and peptides for molecular specific labeling. Significantly improved T/B through AF mitigation enhances the utility of fluorescein-based molecular probes.

Photodegradation of fluorescein was not observed during the multispectral SFE imaging. Since fluorescein is widely reported to undergo rapid photodegradation,[26] we performed a quantitative estimate of fluorescein destruction under the laser illumination levels employed in SFE. We then compared the fluorescein photodegradation rate under the illumination conditions used in a confocal microscope[24] (Table 1). For a 1-mW laser operating at 488 nm, the fluorescein degradation time constant in a confocal microscope is ~240 μs since the laser intensity is much higher than that of the SFE. In contrast to the confocal microscope (spotradius = 0.25 μm), the large spot radius of SFE (25 μm) leads to a much longer (4160×) photodegradation time constant (~1 s); This longer photodegradation time constant, combined with the SFE's short average dwell time of the laser spot on the target (40 ns, or 0.04 μs at 25 MHz sampling rate[45]), yields a very low rate of fluorescein degradation. Therefore, as experimentally observed, the scanning fiber design of the wide-field SFE leads to insignificant photodegradation of fluorescein. This allows more quantitative high-contrast fluorescence imaging to be maintained for the entire fluorescence-guided endoscopic intervention.

In conclusion, we developed and demonstrated a novel approach to evaluate the fluorescence detection sensitivity of a wide-field multispectral SFE for clinical application, such as early esophageal cancer detection and brain tumor delineation. The approach combines the evaluation of device fluorescence detection sensitivity with the quantitative assessment of tissue AF background. A new method, AEC, was developed and applied as a quantitative conversion of the background AF signal to the target fluorophore concentration, such that the

Table 1 Quantitative estimate of fluorescein photodegradation comparison of confocal microscope[24] and scanning fiber endoscope (SFE).

	Confocal microscope	SFE
σ = Fluorescein absorption cross-section	3.06×10^{-16} cm^2/molecule	3.06×10^{-16} cm^2/molecule
Laser (at 488 nm, 1 mW) intensity	1.25×10^{24} photons s^{-1} cm^{-2}, spot radius 0.25 μm	1.25×10^{20} photons s^{-1} cm^{-2}, spot radius 25 μm
K_a = Rate of photon absorption	3.8×10^8 s^{-1}	3.8×10^4 s^{-1}
Q_B = Photobleaching quantum efficiency	3×10^{-5}	3×10^{-5}
K_f = Rate of fluorescence emission (reciprocal of radiative lifetime)	2.2×10^8 s^{-1}	2.2×10^8 s^{-1}
K_B = Rate of photobleaching = $Q_B K_f K_a/(K_f + K_a)$	4.2×10^3 s^{-1}	1.15 s^{-1}
Fluorescein degradation time constant	240 μs	0.9 s
Laser spot dwell time (average)	1 to 10 μs	0.04 μs

background AF can be compared to the target fluorescence. Wide-field SFE fluorescence imaging with nanomolar sensitivity was applied to the delineation of brain tumors in a xenograft mouse model. Finally, high (>80) T/B was observed with a tissue phantom through the implementation of a real-time AF mitigation algorithm using the high-sensitivity multispectral SFE.

Acknowledgments

The study was funded by the National Institutes of Health (NCI grant U54CA163059, PI: T. D. Wang, D. Beer, and E. J. Seibel) as part of the Barrett's Esophagus Translational Research Network (BETRNet). Additional support was provided by NIBIB grant (NIH R01 EB016457, PI: E. J. Seibel) for guided interventions using near-infrared fluorescence imaging. We would like to thank the reviewers for their insightful and constructive comments and suggestion. The authors appreciate Richard Johnson and David Melville at the Human Photonics Lab, University of Washington for their technical support. We would like to thank Dr. James M. Olson at the Fred Hutchison Cancer Research Center, Seattle, for his technical insights and laboratory resources for Tumor Paint™ molecular imaging and the xenograft mouse model. The authors would also like to thank Dr. Thomas D. Wang and his colleagues at the University of Michigan, Ann Arbor, for their suggestions regarding the choice of molecular targets and training in immunofluorescence staining methods, which were used to construct the autofluorescence tissue phantom. The authors would also like to thank Coherent Inc. for the loan of the Galaxy beam combiner and FP lasers.

References

1. M. Goetz and T. D. Wang, "Molecular imaging in gastrointestinal endoscopy," *Gastroenterology* **138**(3), 828–833 (2010).
2. B. C. Wilson, "Detection and treatment of dysplasia in Barrett's esophagus: a pivotal challenge in translating biophotonics from bench to bedside," *J. Biomed. Opt.* **12**(5), 051401 (2007).
3. R. Atreya and M. Goetz, "Molecular imaging in gastroenterology," *Nat. Rev. Gastroenterol. Hepatol.* **10**(12), 704–712 (2013).
4. M. C. Pierce, D. J. Javier, and R. Richards-Kortum, "Optical contrast agents and imaging systems for detection and diagnosis of cancer," *Int. J. Cancer* **123**(9), 1979–1990 (2008).
5. S. F. Elahi and T. D. Wang, "Future and advances in endoscopy," *J. Biophotonics* **4**(7–8), 471–481 (2011).
6. P. J. Pasricha and M. Motamedi, "Optical biopsies, 'bioendoscopy,' and why the sky is blue: the coming revolution in gastrointestinal imaging," *Gastroenterology* **122**(2), 571–575 (2002).
7. M. B. Sturm et al., "Targeted imaging of esophageal neoplasia with a fluorescently labeled peptide: first-in-human results," *Sci. Transl. Med.* **5**(184), 184ra61 (2013).
8. M. Veiseh et al., "Tumor Paint: a chlorotoxin:Cy5.5 bioconjugate for intraoperative visualization of cancer foci," *Cancer Res.* **67**(14), 6882–6888 (2007).
9. Q. T. Nguyen et al., "Surgery with molecular fluorescence imaging using activatable cell-penetrating peptides decreases residual cancer and improves survival," *Proc. Natl. Acad. Sci. USA* **107**(9), 4317–4322 (2010).
10. K. J. Rosbach et al., "Optical molecular imaging of multiple biomarkers of epithelial neoplasia: epidermal growth factor receptor expression and metabolic activity in oral mucosa," *Transl. Oncol.* **5**(3), 160–171 (2012).
11. R. Weissleder et al., "In vivo imaging of tumors with protease-activated near-infrared fluorescent probes," *Nat. Biotechnol.* **17**(4), 375–378 (1999).
12. M. Kriegmair et al., "Detection of early bladder cancer by 5-aminolevulinic acid induced porphyrin fluorescence," *J. Urol.* **155**(1), 105–110 (1996).
13. Z. Liu et al., "In vivo targeting of colonic dysplasia on fluorescence endoscopy with near-infrared octapeptide," *Gut* **62**(3), 395–403 (2013).
14. P.-L. Hsiung et al., "Detection of colonic dysplasia in vivo using a targeted heptapeptide and confocal microendoscopy," *Nat. Med.* **14**(4), 454–458 (2008).
15. G. M. van Dam et al., "Intraoperative tumor-specific fluorescence imaging in ovarian cancer by folate receptor-α targeting: first in-human results," *Nat. Med.* **17**(10), 1315–1319 (2011).
16. S. J. Miller et al., "Targeted detection of murine colonic dysplasia in vivo with flexible multispectral scanning fiber endoscopy," *J. Biomed. Opt.* **17**(2), 021103 (2012).
17. H. Kobayashi et al., "Multimodal nanoprobes for radionuclide and five-color near-infrared optical lymphatic imaging," *ACS Nano* **1**(4), 258–264 (2007).
18. M. Li and T. D. Wang, "Targeted endoscopic imaging," *Gastrointest. Endosc. Clin. N. Am.* **19**(2), 283–298 (2009).
19. M. S. Hoetker and M. Goetz, "Molecular imaging in endoscopy," *United European Gastroenterol. J.* **1**(2), 84–92 (2013).
20. R. S. DaCosta, B. C. Wilson, and N. E. Marcon, "Spectroscopy and fluorescence in esophageal," *Best Pract. Res. Clin. Gastroenterol.* **20**(1), 41–57 (2006).
21. J. V. Frangioni, "New technologies for human cancer imaging," *J. Clin. Oncol.* **26**(24), 4012–4021 (2008).

22. J. T. C. Liu et al., "Quantifying cell-surface biomarker expression in thick tissues with ratiometric three-dimensional microscopy," *Biophys. J.* **96**(6), 2405–2414 (2009).
23. H. S. Choi et al., "Targeted zwitterionic near-infrared fluorophores for improved optical imaging," *Nat. Biotechnol.* **31**(2), 148–153 (2013).
24. R. Y. Tsien, L. Ernst, and A. Waggoner, "Fluorophores for confocal microscopy: photophysics and photochemistry," in *Handbook of Biological Confocal Microscopy*, J. B. Pawley, Ed., pp. 338–352, Springer, New York, NY (2006).
25. M. S. T. Goncalves, "Fluorescent labeling of biomolecules with organic probes," *Chem. Rev.* **109**(1), 190–212 (2009).
26. R. Y. Tsien, "Fluorescent indicators of ion concentrations," in *Methods in Cell Biology*, L. Wilson and P. Tran, Eds., Vol. 30, pp. 127–156, Academic Press, Waltham, Massachusetts (1989).
27. Q. T. Nguyen and R. Y. Tsien, "Fluorescence-guided surgery with live molecular navigation—a new live cutting edge," *Nat. Rev.* **13**(9), 653–662 (2013).
28. R. Weissleder and M. J. Pittet, "Imaging in the era of molecular oncology," *Nature* **452**(7187), 580–589 (2008).
29. R. Alford et al., "Toxicity of organic fluorophores used in molecular imaging: literature review," *Mol. Imaging* **8**(6), 341–354 (2009).
30. J. Gao, P. Wang, and R. W. Giese, "Xanthamide fluorescent dyes," *Anal. Chem.* **74**(24), 6397–6401 (2002).
31. O. N. Burchak et al., "Fluorescein-based amino acids for solid phase synthesis of fluorogenic protease substrates," *Bioorg. Med. Chem.* **14**(8), 2559–2568 (2006).
32. V. Venugopal et al., "Design and characterization of an optimized simultaneous color and near-infrared fluorescence rigid endoscopic imaging system," *J. Biomed. Opt.* **18**(12), 126018 (2013).
33. A. Bogaards, H. Sterenborg, and B. C. Wilson, "In vivo quantification of fluorescent molecular markers in real-time: a review to evaluate the performance of five existing methods," *Photodiagnosis Photodyn. Ther.* **4**(3), 170–178 (2007).
34. R. Baumgartner et al., "A fluorescence imaging device for endoscopic detection of early stage cancer—instrumental and experimental studies," *Photochem. Photobiol.* **46**(5), 759–763 (1987).
35. T. Troy et al., "Quantitative comparison of the sensitivity of detection of fluorescent and bioluminescent reporters in animal models," *Mol. Imaging* **3**(1), 9–23 (2004).
36. P. B. Garcia-Allende et al., "Towards clinically translatable NIR fluorescence molecular guidance for colonoscopy," *Biomed. Opt. Express* **5**(1), 78–92 (2014).
37. F. Fantoni et al., "Background fluorescence reduction and absorption correction for fluorescence reflectance imaging," *Proc. SPIE* **8935**, 89350Z (2014).
38. R. A. Sheth, L. Josephson, and U. Mahmood, "Evaluation and clinically relevant applications of a fluorescent imaging analog to fluorodeoxyglucose positron emission tomography," *J. Biomed. Opt.* **14**(6), 064014 (2009).
39. N. Thekkek et al., "Pre-clinical evaluation of fluorescent deoxyglucose as a topical contrast agent for the detection of Barrett's-associated neoplasia during confocal imaging," *Technol. Cancer Res. Treat.* **10**(5), 431–441 (2011).
40. N. Nitin et al., "Molecular imaging of glucose uptake in oral neoplasia following topical application of fluorescently labeled deoxy-glucose," *Int. J. Cancer* **124**(11), 2634–2642 (2009).
41. Y. Liu et al., "Near-infrared fluorescence goggle system with complementary metal–oxide–semiconductor imaging sensor and see-through display," *J. Biomed. Opt.* **18**(10), 101303 (2013).
42. J. Glatz et al., "Concurrent video-rate color and near-infrared fluorescence laparoscopy," *J. Biomed. Opt.* **18**(10), 101302 (2013).
43. C. Azzi et al., "Permeation and reservoir formation of 4-(methylnitrosamino)-1-(3-pyridyl)-1-butanone (NNK) and benzo[a]pyrene (B[a]P) across porcine esophageal tissue in the presence of ethanol and menthol," *Carcinogenesis* **27**(1), 137–145 (2005).
44. C. Yang et al., "Scanning fiber endoscope with multiple fluorescence-reflectance imaging channels for guiding biopsy," *Proc. SPIE* **8936**, 89360R (2014).
45. C. M. Lee et al., "Scanning fiber endoscopy with highly flexible, 1 mm catheterscopes for wide-field, full-color imaging," *J. Biophotonics* **3**(5–6), 385–407 (2010).
46. M. R. Stroud, S. J. Hansen, and J. M. Olson, "In vivo bio-imaging using chlorotoxin-based conjugates," *Curr. Pharm. Des.* **17**(38), 4362–4371 (2011).
47. V. W. Hou et al., "The development of a simplified epithelial tissue phantom for the evaluation of an autofluorescence mitigation algorithm," *Proc. SPIE* **8945**, 894506 (2014).
48. Coherent Inc., "OBIS Galaxy—laser beam combiner," 2014, http://www.coherent.com/products/?2080/OBIS-Galaxy (14 February 2014).
49. C. Yang et al., "Multispectral scanning fiber endoscope with concurrent autofluorescence background mitigation for improved target-to-background ratio," *Proc. SPIE* **8927**, 89270I (2014).
50. C. Yang et al., "Color-matched and fluorescence-labeled esophagus phantom and its applications," *J. Biomed. Opt.* **18**(2), 026020 (2013).
51. C. Yang et al., "Mitigating fluorescence spectral overlap in wide-field endoscopic imaging," *J. Biomed. Opt.* **18**(8), 086012 (2013).
52. M. A. Kara et al., "Characterization of tissue autofluorescence in Barrett's esophagus by confocal fluorescence microscopy," *Dis. Esophagus* **20**(2), 141–150 (2007).
53. S. R. Rantelhardt et al., "Imaging of brain and brain tumor specimens by time-resolved multiphoton excitation microscopy ex vivo," *Neuro Oncol.* **9**(2), 103–112 (2007).
54. S. K. Chapman and G. A. Reid, "UV-visible spectroscopy as a tool to study flavoproteins," in *Flavoprotein Protocols*, S. K. Chapman and G. A. Reid, Eds., pp. 1–7, Humana Press Inc., Totowa, New Jersey (1999).
55. J. A. Lewis and J. C. Escalante-Semerena, "The FAD-dependent tricarballylate dehydrogenase (TcuA) enzyme of Salmonella enterica converts tricarballylate into cis-aconitate," *J. Bacteriol.* **188**(15), 5479–5486 (2006).
56. S. Prahl, "Riboflavin," 5 May 2012, http://omlc.ogi.edu/spectra/PhotochemCAD/html/004.html (11 June 2014).
57. R. S. DaCosta, H. Andersson, and B. C. Wilson, "Molecular fluorescence excitation–emission matrices relevant to tissue spectroscopy," *Photochem. Photobiol.* **78**(4), 384–392 (2003).
58. H. D. Vishwasrao et al., "Conformational dependence of intracellular NADH on metabolic state revealed by associated fluorescence anisotropy," *J. Biol. Chem.* **280**(26), 25119–25126 (2005).
59. C. H. van de Lest et al., "Elimination of autofluorescence in immunofluorescence microscopy with digital image processing," *J. Histochem. Cytochem.* **43**(7), 727–730 (1995).
60. M. Zellweger et al., "Absolute autofluorescence spectra of human healthy, metaplastic, and early cancerous bronchial tissue in vivo," *Appl. Opt.* **40**(22), 3784–3791 (2001).
61. H. Chung et al., "Evaluation of surface and build-up region dose for intensity-modulated radiation therapy in head and neck cancer," *Med. Phys.* **32**(8), 2682–2689 (2005).
62. S. Prahl, "Optical absorption of hemoglobin," 15 December 1999, http://omlc.ogi.edu/spectra/hemoglobin/ (30 January 2014).
63. H. S. Choi et al., "Synthesis and in vivo fate of zwitterionic near-infrared fluorophores," *Angew. Chem. Int. Ed. Engl.* **50**(28), 6258–6263 (2011).

Biographies of the authors are not available.